Acta Mechanica manuscript No.
(will be inserted by the editor)

M.J. Dai · S. Tanaka · S. Oterkus · E. Oterkus

Static and dynamic mechanical behaviors of cracked Mindlin plates in ordinary state-based peridynamic framework

Received: date / Accepted: date

Abstract An ordinary state-based peridynamic (PD) model based on the Mindlin plate theory is presented to deal with fracture mechanics problems. Static and dynamic stress resultant intensity factors regarded as the primary fracture parameters for plate structures are evaluated by the displacement extrapolation method. Owing to the PD surface effect, however, the accuracy of the displacement field near crack surfaces is significantly affected. Therefore, the arbitrary horizon domain method is adopted to correct the surface effect. It derives the variable PD parameters to properly describe mechanical behaviors for each material point. Several numerical examples are investigated to examine the performance of the presented method. It indicates that the PD Mindlin plate model incorporated with the arbitrary horizon domain method validly minimizes the influence from the PD surface effect and provides an effective approach to evaluate static and dynamic moment intensity factors.

Keywords Peridynamics · Plate structures · Arbitrary horizon domain · PD surface effect · Moment intensity factors

1 Introduction

Peridynamics (PD) [1,2], which does not require spatial derivatives in its governing equations, has been developed to simulate different kinds of complicated fracture problems. For thin-walled structures, a shell model is an effective approach with less computation time than a 3D solid model. In the shell model, 2D plane stress and plate bending formulae are adopted to treat in-plane and out-of-plane deformations, respectively. However, in contrast to 2D plane stress problems, the studies in plate bending problems are relatively few in the PD literature. O'Grady and Foster derived a non-ordinary state-based peridynamic (NOSPD) model for Kirchhoff-Love plates [3] and shells [4] from the concept of rotational springs between interaction bonds. Diyaroglu et al. [5] developed a bond-based peridynamic (BBPD) model for beams and plates with transverse shear deformation. Chowdhury et al. [6] introduced a surface-based NOSPD model with curved bonds for linear elastic shells. Nguyen

M.J. Dai
Graduate School of Advanced Science and Engineering, Hiroshima University, Japan
E-mail: mingjyundai@gmail.com

S. Tanaka
Graduate School of Advanced Science and Engineering, Hiroshima University, Japan
E-mail: satoyuki@hiroshima-u.ac.jp

S. Oterkus
Department of Naval Architecture, Ocean and Marine Engineering, University of Strathclyde, United Kingdom
E-mail: selda.oterkus@strath.ac.uk

E. Oterkus
Department of Naval Architecture, Ocean and Marine Engineering, University of Strathclyde, United Kingdom
E-mail: erkan.oterkus@strath.ac.uk

and Oterkus [7] proposed a three-dimensional shell model with six degrees of freedom in ordinary state-based peridynamics (OSPD). Yang et al. presented Kirchhoff plate [8] and higher-order plate [9] models in OSPD with various boundary conditions (BCs). Zhang et al. [10] developed a nonlinear Reissner-Mindlin shell model in NOSPD. Nguyen and Oterkus [11] investigated a geometrically nonlinear analysis of plate bending problems in OSPD. Shen et al. proposed PD beam and shell models based on micro-beam bonds obtained via the interpolation method [12,13]. Zhang et al. [14] derived a nonlocal geometrically-exact shell model by using nonlocal differential operators.

The PD surface effect arises from the assumption that the PD parameters computed under a complete circle/sphere horizon are constant for each material point. If the material point is located near domain boundaries or crack surfaces, it does not possess a complete horizon. Meanwhile, the constant PD parameters cannot correctly reproduce mechanical behaviors. Several correction methods have been proposed to reduce the PD surface effect. Le and Bobaru [15] discussed in detail the capability of the different surface effect corrections for elastic and fracture problems. An alternative concept for PD surface effect correction that derives the variable PD parameters computed under its current horizon domain for each material point was presented [16,17]. However, those studies only concentrated on 2D plane problems. Dai et al. [18] proposed a similar approach with arbitrary horizon domains, called the arbitrary horizon domain method, in computations of the PD parameters to assess crack opening displacements (CODs) and strain energy densities for shell structures.

J-integral and stress intensity factors (SIFs) utilized in most previous numerical and experimental studies are regarded as the primary fracture quantities to determine crack extension. Silling and Lehoucq [19] firstly presented a nonlocal J-integral formulation in the state-based PD framework. Hu et al. [20] subsequently proposed a convergence analysis of the PD J-integral in BBPD. Le and Bobaru [15] investigated the performance of the different surface effect corrections in PD J-integral evaluation. Stenström and Eriksson developed the contour [21] and domain [22] forms of the PD J-integral based on the displacement field in BBPD. Those studies mentioned above only discussed mode-I fracture conditions. For mixed-mode fracture conditions, Imachi et al. [23,24] evaluated dynamic SIFs for 2D elastic cracked solids. Dai et al. assessed SIFs for shell structures subjected to in-plane [25] and out-of-plane [26] loading.

To the authors' knowledge, the evaluation of static stress resultant intensity factors (SRIFs) for plate bending problems [26] had been merely carried out once in the PD literature. In addition, the evaluation of dynamic SRIFs has still not been discussed. Hence, the Mindlin plate model in the OSPD framework [7] is presented to treat fracture mechanics problems. Static and dynamic moment intensity factors are assessed by employing the displacement extrapolation method [27,28]. To minimize the influence from the PD surface effect near crack surfaces, the arbitrary horizon domain method [18] is adopted in computations of the PD parameters. Meanwhile, two additional PD approaches are considered to compare with the proposed surface effect correction; specifically, the standard PD method without correction and the volume method [29]. Several numerical examples are investigated, including static and dynamic loading conditions, to examine the accuracy of the proposed method. Notably, the pressure load, which is the major loading mode in aerospace and maritime structures, is applied to most of the numerical examples in the present study.

The remainder of this study is organized as follows: The PD Mindlin plate model and its numerical implementations are introduced in Section 2. The arbitrary horizon domain method and the displacement extrapolation method are presented in Section 3. Several numerical problems are examined to verify the proposed method in Section 4. Lastly, the summaries and conclusions are discussed in Section 5.

2 Ordinary state-based peridynamic theory

2.1 Peridynamic model for plate structures

The OSPD model based on the Mindlin plate theory [7] is employed in the present study. Each material point $\boldsymbol{x}$ interacts with other material points $\boldsymbol{x}'$ within a constant distance, δ. The non-local region is referred to as the horizon, and the material points within δ are called the family of $\boldsymbol{x}$, $H_{\boldsymbol{x}}$. Material behavior in the PD theory is prescribed through nonlocal interactions between material points.

A schematic illustration of the PD plate model is presented in Fig. 1. $\boldsymbol{x}_{(k)}$ denotes the initial position of point k, and $\boldsymbol{y}_{(k)}$ denotes the deformed position of point k. φ represents the angle of the

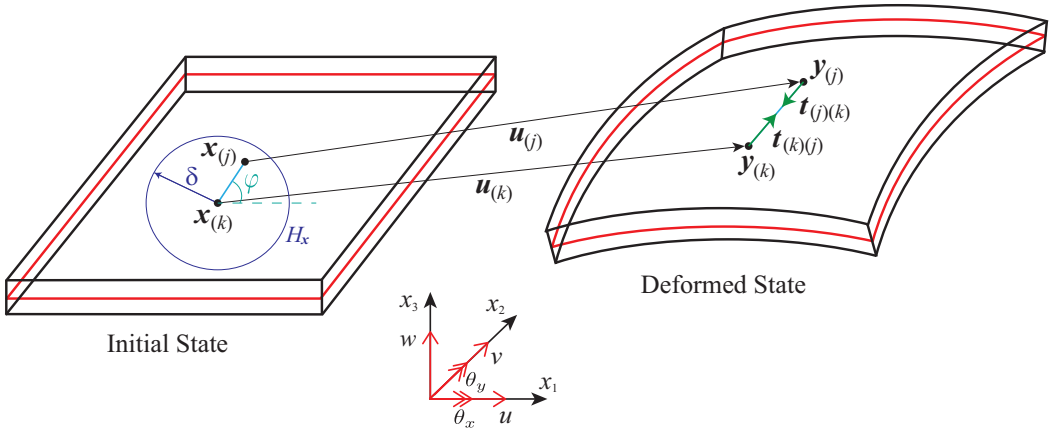

Fig. 1 Initial and deformed states of a plate structure.

interaction bond with respect to the x_1-axis. h is the plate thickness, and δ is the horizon radius. $\boldsymbol{u}_{(k)}$=$[u\ v\ w\ \theta_x\ \theta_y]^T$ indicates the displacement vector of point k. $\boldsymbol{t}_{(k)(j)}$ and $\boldsymbol{t}_{(j)(k)}$ signify the PD force density vectors between points k and j. Note that the small deformation assumption is taken into account in the proposed PD model.

The strain energy density in PD is defined as a summation of micro-potentials arising from the interactions between material points within H_x. Furthermore, the micro-potential depends on the constitutive properties and bond deformation of each interaction bond. The strain energy densities for the bending and transverse shear terms in the proposed OSPD model are defined as:

$$\bar{W}^{PD}_{b(k)} = a_b \vartheta^2_{b(k)} + b_b \sum_{j=1}^{N} \underline{w} s^2_{b(k)(j)} \xi^2 V_{(j)}, \tag{1}$$

$$\bar{W}^{PD}_{s(k)} = \frac{1}{4} C_s \sum_{j=1}^{N} \underline{w} \left(\frac{w_{(j)} - w_{(k)}}{\xi} - \frac{\bar{\theta}_{(j)} + \bar{\theta}_{(k)}}{2} \right)^2 \xi^2 V_{(j)}. \tag{2}$$

The terms $s_{b(k)(j)}$ and $\vartheta_{b(k)}$ in Eq. (1) are defined as:

$$s_{b(k)(j)} = \frac{-(\theta_{y(j)} - \theta_{y(k)}) \cos\varphi + (\theta_{x(j)} - \theta_{x(k)}) \sin\varphi}{\xi}, \tag{3}$$

$$\vartheta_{b(k)} = d_b \sum_{j=1}^{N} \underline{w} s_{b(k)(j)} \xi V_{(j)}. \tag{4}$$

The terms $\bar{\theta}_{(k)}$ and $\bar{\theta}_{(j)}$ in Eq. (2) are defined as:

$$\bar{\theta}_{(k)} = -\theta_{y(k)} \cos\varphi + \theta_{x(k)} \sin\varphi, \tag{5}$$

$$\bar{\theta}_{(j)} = -\theta_{y(j)} \cos\varphi + \theta_{x(j)} \sin\varphi, \tag{6}$$

where the influence function $\underline{w}$ is defined as δ/ξ. ξ denotes the distance between points k and j. N indicates the total number of interactions between material points within H_x. a, b, d, and C mentioned

above represent the PD parameters. Subscripts b and s indicate the bending and transverse shear terms, respectively.

By comparing ϑ_b, $\bar{W}_b$, and $\bar{W}_s$ between CCM and PD under the assumption that the material point possesses a complete horizon, the constant PD parameters for each material point can be obtained. The PD parameters for the bending and transverse shear terms are expressed as:

$$a_b = \frac{Eh^3(3\nu - 1)}{48(1-\nu^2)}, \quad d_b = \frac{Eh^2}{4\pi\delta^4(1+\nu)}, \quad b_b = \frac{2}{\pi h\delta^3}, \tag{7}$$

$$C_s = \frac{3k_sE}{\pi\delta^4(1+\nu)}, \tag{8}$$

where E and ν denote Young's modulus and Poisson's ratio, respectively. k_s represents the shear correction factor.

The PD equation of motion for the Mindlin plate model is derived by substituting kinetic and potential energies into the Euler-Lagrange equation. It is expressed in an integro-differential form without spatial derivatives as:

$$\boldsymbol{m}_{(k)}\ddot{\boldsymbol{u}}_{(k)} = \sum_{j=1}^{N} \mu_{(k)(j)}\boldsymbol{f}_{(k)(j)}V_{(j)} + \boldsymbol{b}_{(k)}, \tag{9}$$

where $\boldsymbol{m}_{(k)}$ and $\ddot{\boldsymbol{u}}_{(k)}$ denote the mass matrix and acceleration vector, respectively. $\boldsymbol{f}_{(k)(j)}$ and $\boldsymbol{b}_{(k)}$ represent the PD force density vector and body force density vector, respectively. $V_{(j)}$ indicates the volume of point j. $\mu_{(k)(j)}$ signifies the state of each interaction bond. Crack segments can be easily modeled by the status of interaction bonds (see Fig. 2). $\mu_{(k)(j)}$ is defined as:

$$\mu_{(k)(j)} = \begin{cases} 0 & \text{broken bond} \\ 1 & \text{intact bond} \end{cases} \tag{10}$$

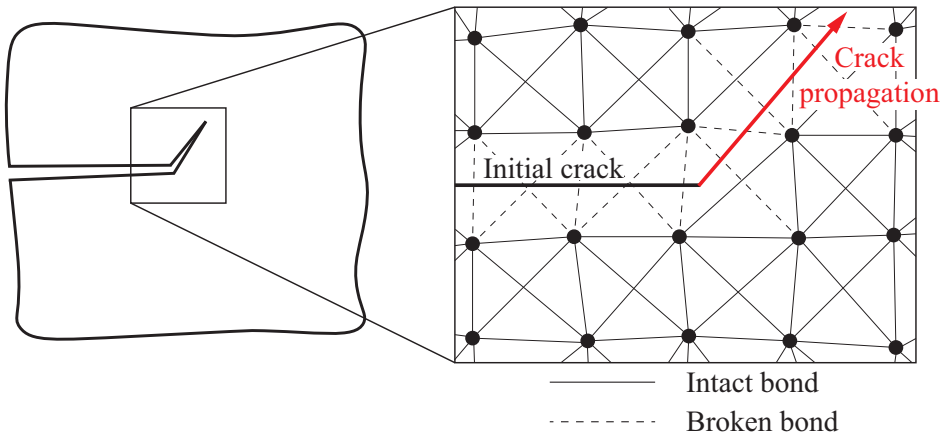

Fig. 2 Schematic illustration of interaction bond states for crack modeling (δ=1.5Δx).

According to the derivation of the PD equation of motion, the PD force densities for each degree of freedom in the Mindlin plate model are expressed as:

$$
\begin{aligned}
f^{w}_{(k)(j)} =& C_s \underline{w}\{\frac{w_{(j)} - w_{(k)}}{\xi} - \frac{1}{2}[-(\theta_{y(k)} + \theta_{y(j)})\cos\varphi \\
&+ (\theta_{x(k)} + \theta_{x(j)})\sin\varphi]\}\xi,
\end{aligned} \tag{11}
$$

$$
\begin{aligned}
f^{\theta_x}_{(k)(j)} =& [2a_b d_b \underline{w}(\vartheta_{b(k)} + \vartheta_{b(j)}) + 4b_b \underline{w} s_{b(k)(j)}\xi]\sin\varphi \\
&+ \frac{1}{2} C_s \underline{w}\{(w_{(j)} - w_{(k)})\sin\varphi \\
&- \frac{\xi}{2}[-(\theta_{y(k)} + \theta_{y(j)})\sin\varphi\cos\varphi + (\theta_{x(k)} + \theta_{x(j)})\sin^2\varphi]\}\xi,
\end{aligned} \tag{12}
$$

$$
\begin{aligned}
f^{\theta_y}_{(k)(j)} =& -[2a_b d_b \underline{w}(\vartheta_{b(k)} + \vartheta_{b(j)}) + 4b_b \underline{w} s_{b(k)(j)}\xi]\cos\varphi \\
&- \frac{1}{2} C_s \underline{w}\{(w_{(j)} - w_{(k)})\cos\varphi \\
&- \frac{\xi}{2}[-(\theta_{y(k)} + \theta_{y(j)})\cos^2\varphi + (\theta_{x(k)} + \theta_{x(j)})\sin\varphi\cos\varphi]\}\xi.
\end{aligned} \tag{13}
$$

2.2 Adaptive dynamic relaxation method for static simulations

Although the PD equation of motion is in a dynamic form, static and quasi-static problems in PD can be solved via the adaptive dynamic relaxation (ADR) technique [30,31]. By introducing the fictitious mass and damping terms, the PD equation of motion in the ADR method can be rewritten as:

$$
\boldsymbol{D}\ddot{\boldsymbol{U}}(\boldsymbol{X}, t) + c\boldsymbol{D}\dot{\boldsymbol{U}}(\boldsymbol{X}, t) = \boldsymbol{F}(\boldsymbol{U}, \boldsymbol{U}', \boldsymbol{X}, \boldsymbol{X}'), \tag{14}
$$

where $\boldsymbol{D}$ is the fictitious diagonal density matrix, and c is the damping coefficient. $\boldsymbol{X}$ and $\boldsymbol{U}$ denote the initial position and displacement vectors, respectively. The force vector $\boldsymbol{F}$ composed of PD interaction forces and body forces is expressed as:

$$
\boldsymbol{F}_{(i)} = \sum_{j=1}^{N} (\boldsymbol{t}_{(i)(j)} - \boldsymbol{t}_{(j)(i)}) V_{(j)} + \boldsymbol{b}_{(i)}. \tag{15}
$$

By applying the central-difference scheme, the velocity $\dot{\boldsymbol{U}}^{n+1/2}$ and displacement $\boldsymbol{U}^{n+1}$ vectors for the next time step can be approximated as:

$$
\dot{\boldsymbol{U}}^{n+1/2} = \frac{(2 - c^n \Delta t)\dot{\boldsymbol{U}}^{n-1/2} + 2\Delta t \boldsymbol{D}^{-1}\boldsymbol{F}^n}{2 + c^n \Delta t}, \tag{16}
$$

$$
\boldsymbol{U}^{n+1} = \boldsymbol{U}^n + \Delta t \dot{\boldsymbol{U}}^{n+1/2}, \tag{17}
$$

where n indicates the *n-th* iteration. Δt represents the time step, and Δt=1 is a common choice in the ADR method.

Because of the unknown velocity vector $\dot{\boldsymbol{U}}^{-1/2}$, the velocity vector $\dot{\boldsymbol{U}}^{1/2}$ cannot be obtained at the initial time step (n=0) by using Eq. (16). Therefore, the iteration can be started by:

$$
\dot{\boldsymbol{U}}^{1/2} = \frac{\Delta t \boldsymbol{D}^{-1}\boldsymbol{F}^0}{2}. \tag{18}
$$

The damping coefficient c^n can be expressed in a similar manner to the lowest frequency discussed in Ref. [32] as:

$$c^n = 2\sqrt{((\boldsymbol{U}^n)^T {}^1\boldsymbol{K}^n \boldsymbol{U}^n)/((\boldsymbol{U}^n)^T \boldsymbol{U}^n)}, \tag{19}$$

$${}^1K^n_{(i)(i)} = -(F^n_{(i)}/\lambda_{(i)(i)} - F^{n-1}_{(i)}/\lambda_{(i)(i)})/(\Delta t \dot{u}^{n-1/2}_{(i)}), \tag{20}$$

where ${}^1\boldsymbol{K}^n$ and ${}^1K^n_{(i)(i)}$ are the diagonal local stiffness matrix and its diagonal element, respectively. $\lambda_{(i)(i)}$ denotes the diagonal element of the density matrix $\boldsymbol{D}$. For the PD Mindlin plate model, $\lambda_{(i)(i)}$ was defined in Ref. [7].

2.3 Central-difference explicit method for dynamic simulations

The central-difference explicit scheme is employed in the PD framework to deal with dynamic problems. In contrast to Eq. (14), the PD equation of motion without a damping term is written as:

$$\boldsymbol{m}\ddot{\boldsymbol{u}}^n_{(i)} = \sum_{j=1}^{N} (\boldsymbol{t}^n_{(i)(j)} - \boldsymbol{t}^n_{(j)(i)}) V_{(j)} + \boldsymbol{b}^n_{(i)}. \tag{21}$$

In the central-difference explicit scheme, the acceleration vector $\ddot{\boldsymbol{u}}^n_{(i)}$ is given by:

$$\ddot{\boldsymbol{u}}^n_{(i)} = \frac{\boldsymbol{u}^{n+1}_{(i)} - 2\boldsymbol{u}^n_{(i)} + \boldsymbol{u}^{n-1}_{(i)}}{\Delta t^2}, \tag{22}$$

where n indicates the n-th time step, and Δt represents the time step.

By substituting Eq. (22) into Eq. (21) and after some algebraic manipulations, the displacement vector $\boldsymbol{u}^{n+1}_{(i)}$ for the next time step can be approximated as:

$$\boldsymbol{u}^{n+1}_{(i)} = \frac{\Delta t^2}{\boldsymbol{m}} [\sum_{j=1}^{N} (\boldsymbol{t}^n_{(i)(j)} - \boldsymbol{t}^n_{(j)(i)}) V_{(j)} + \boldsymbol{b}^n_{(i)}] + 2\boldsymbol{u}^n_{(i)} - \boldsymbol{u}^{n-1}_{(i)}. \tag{23}$$

Similarly, the displacement vector $\boldsymbol{u}^1_{(i)}$ cannot be obtained at the initial time step (n=0) by using Eq. (23) due to the unknown displacement vector $\boldsymbol{u}^{-1}_{(i)}$. To compute the displacement vector $\boldsymbol{u}^{-1}_{(i)}$, the backward difference method is applied [33].

3 Stress resultant intensity factor evaluation

To evaluate static and dynamic SRIFs, the displacement extrapolation method [27,28,34] based on the displacement field around the crack tip is applied. It provides a simple approach with reasonable accuracy for assessing SIFs and SRIFs. However, the PD surface effect remarkably affects the accuracy of mechanical behaviors near crack surfaces. The error distribution of the near-tip displacement field between the PD and analytical solutions is illustrated in Fig. 3(a). It indicates that the major errors, whose maximum value reaches over 30 %, are observed along the crack surface. Therefore, the arbitrary horizon domain method [18] is adopted to treat the influence from the PD surface effect. Here, the arbitrary horizon domain method and the displacement extrapolation method are introduced.

3.1 Arbitrary horizon domain method for PD parameters

In the standard PD approach, the PD parameters computed on the basis of a complete circle/sphere horizon are constant for each material point. The constant PD parameters cannot correctly reproduce mechanical behaviors when the material point located near domain boundaries or crack surfaces does not possess a complete horizon. The arbitrary horizon domain method employs the actual influence domains in computations of the PD parameters, as expressed in Fig. 3(b), which are similar to the visibility criterion [35] in the meshfree method. By comparing ϑ_b, $\bar{W}_b$, and $\bar{W}_s$ assessed within the actual horizon domain between CCM and PD under simple loading conditions, the variable PD parameters can be derived. The derivation of the variable PD parameters is presented in this subsection.

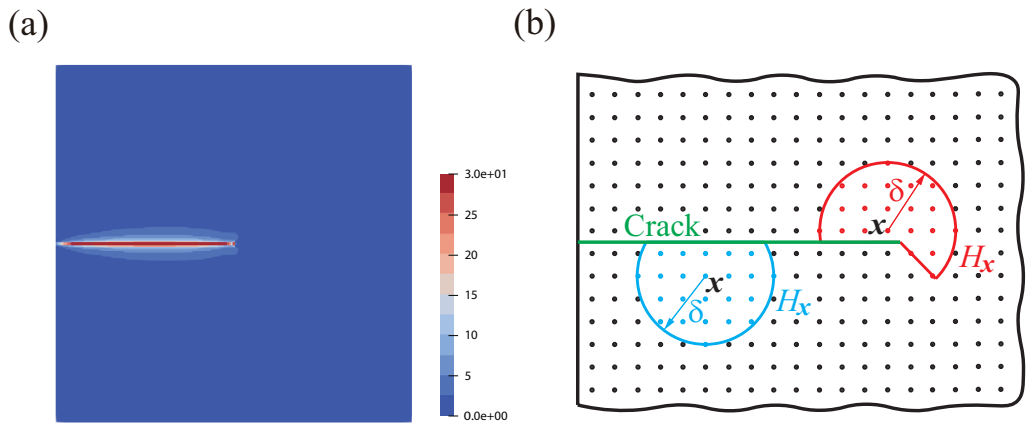

Fig. 3 (a) Relative error distribution (%) of the near-tip displacement field, (b) Arbitrary horizon domains near crack surfaces.

By using Taylor's series expansion and ignoring the higher-order terms, the transverse deflection and rotation components of point j are expressed as:

$$\begin{aligned} w_{(j)} &= w_{(k)} + w_{,x(k)}(x_{(j)} - x_{(k)}) + w_{,y(k)}(y_{(j)} - y_{(k)}), \\ \theta_{x(j)} &= \theta_{x(k)} + \theta_{x,x(k)}(x_{(j)} - x_{(k)}) + \theta_{x,y(k)}(y_{(j)} - y_{(k)}), \\ \theta_{y(j)} &= \theta_{y(k)} + \theta_{y,x(k)}(x_{(j)} - x_{(k)}) + \theta_{y,y(k)}(y_{(j)} - y_{(k)}), \end{aligned} \tag{24}$$

which can be rewritten as:

$$\begin{aligned} \frac{w_{(j)} - w_{(k)}}{\xi} &= w_{,x(k)} \cos\varphi + w_{,y(k)} \sin\varphi, \\ \frac{\theta_{x(j)} - \theta_{x(k)}}{\xi} &= \theta_{x,x(k)} \cos\varphi + \theta_{x,y(k)} \sin\varphi, \\ \frac{\theta_{y(j)} - \theta_{y(k)}}{\xi} &= \theta_{y,x(k)} \cos\varphi + \theta_{y,y(k)} \sin\varphi. \end{aligned} \tag{25}$$

An alternative form of s_b is expressed by substituting two rotation components in Eq. (25) into Eq. (3) as:

$$s_{b(k)(j)} = -\theta_{y,x(k)} \cos^2\varphi - \theta_{y,y(k)} \sin\varphi \cos\varphi + \theta_{x,x(k)} \sin\varphi \cos\varphi + \theta_{x,y(k)} \sin^2\varphi. \tag{26}$$

The PD parameters a_b and d_b are obtained by comparing $\bar{W}_b$ and ϑ_b between PD and CCM under the isotropic bending condition, respectively. The term ϑ_b^{PD} in Eq. (4) under the isotropic bending condition ($-\theta_{y,x(k)}=\zeta$, $\theta_{x,y(k)}=\zeta$) becomes

$$\begin{aligned}\vartheta_{b(k)}^{PD} =& d_b h \int_{H_x} \underline{w} s_{b(k)(j)} \xi dA \\ =& d_b h \int_{H_x} \underline{w} \zeta \xi dA.\end{aligned} \tag{27}$$

The term ϑ_b^{CCM} under the isotropic bending condition becomes

$$\vartheta_{b(k)}^{CCM} = 2\zeta. \tag{28}$$

Equating the terms ϑ_b between Eqs. (27) and (28) yields the PD parameter d_b as:

$$d_b = \frac{2}{h \int_{H_x} \underline{w} \xi dA}. \tag{29}$$

Similarly, the term $\bar{W}_b^{PD}$ in Eq. (1) under the isotropic bending condition ($-\theta_{y,x(k)}=\zeta$, $\theta_{x,y(k)}=\zeta$, and $\vartheta_{b(k)}=2\zeta$) becomes

$$\begin{aligned}\bar{W}_{b(k)}^{PD} =& a_b \vartheta_{b(k)}^2 + b_b h \int_{H_x} \underline{w} s_{b(k)(j)}^2 \xi^2 dA \\ =& a_b (2\zeta)^2 + b_b h \int_{H_x} \underline{w} \zeta^2 \xi^2 dA.\end{aligned} \tag{30}$$

The term $\bar{W}_b^{CCM}$ under the isotropic bending condition becomes

$$\bar{W}_{b(k)}^{CCM} = \frac{Eh^3}{12(1-\nu)} \zeta^2. \tag{31}$$

Equating the terms $\bar{W}_b$ between Eqs. (30) and (31) yields the PD parameter a_b as:

$$a_b = \frac{Eh^3}{48(1-\nu)} - \frac{b_b h}{4} \int_{H_x} \underline{w} \xi^2 dA. \tag{32}$$

The PD parameter b_b is obtained by comparing $\bar{W}_b$ between PD and CCM under the torsion condition. The term $\bar{W}_b^{PD}$ in Eq. (1) under the torsion condition ($-\theta_{y,y(k)}=\zeta$, $\theta_{x,x(k)}=\zeta$, and $\vartheta_{b(k)}=0$) becomes

$$\begin{aligned}\bar{W}_{b(k)}^{PD} =& b_b h \int_{H_x} \underline{w} s_{b(k)(j)}^2 \xi^2 dA \\ =& b_b h \int_{H_x} \underline{w} (\zeta \sin\varphi \cos\varphi)^2 \xi^2 dA.\end{aligned} \tag{33}$$

The term $\bar{W}_b^{CCM}$ under the torsion condition becomes

$$\bar{W}_{b(k)}^{CCM} = \frac{Eh^3}{48(1+\nu)} \zeta^2. \tag{34}$$

Equating the terms $\bar{W}_b$ between Eqs. (33) and (34) yields the PD parameter b_b as:

$$b_b = \frac{Eh^2}{48(1+\nu)} \frac{1}{\int_{H_x} \underline{w} (\xi \cos\varphi \sin\varphi)^2 dA}. \tag{35}$$

The PD parameter C_s is obtained by comparing $\bar{W}_s$ between PD and CCM under the transverse shear condition. The term $\bar{W}_s^{PD}$ in Eq. (2) that assumes $\bar{\theta}_{(k)}$=$\bar{\theta}_{(j)}$ under the transverse shear condition ($(w_{,x}+\theta_y)=\zeta$, $(w_{,y}-\theta_x)=\zeta$) becomes

$$\begin{aligned}\bar{W}_{s(k)}^{PD} =&\frac{1}{4}C_s h\int_{H_x}\underline{w}(\frac{w_{(j)}-w_{(k)}}{\xi}-\bar{\theta}_{(k)})^2\xi^2 dA\\ =&\frac{1}{4}C_s h\int_{H_x}\underline{w}\zeta^2\xi^2 dA.\end{aligned} \tag{36}$$

The term $\bar{W}_s^{CCM}$ under the transverse shear condition becomes

$$\bar{W}_{s(k)}^{CCM}=\frac{k_s E h}{2(1+\nu)}\zeta^2. \tag{37}$$

Equating the terms $\bar{W}_s$ between Eqs. (36) and (37) yields the PD parameter C_s as:

$$C_s=\frac{k_s E}{1+\nu}\frac{2}{\int_{H_x}\underline{w}\xi^2 dA}. \tag{38}$$

The PD parameters in the proposed method are exactly the same as those in Eqs. (7) and (8) through integrating the integrand over the complete circle horizon. It confirms that the derivation of the PD parameters is properly conducted in the arbitrary horizon domain method. Moreover, the volume correction technique [31] is adopted in computations of the variable PD parameters.

3.2 Crack surface displacement extrapolation method

The displacement extrapolation method is employed to assess static and dynamic moment/shear intensity factors for plate structures. It is based on the asymptotic displacement field around the crack tip. The asymptotic displacement field of the Mindlin-Reissner plate theory [36,37] that only retains the terms depending on $r'^{1/2}$ is presented as:

$$\begin{aligned}w=&\frac{24(1+\nu)}{5Eh}\sqrt{\frac{r'}{2}}K_3\sin\frac{\theta'}{2},\\ \theta_x=&\frac{12(1+\nu)}{Eh^3}\sqrt{\frac{r'}{2}}[K_1\sin\frac{\theta'}{2}(\frac{\nu-3}{1+\nu}+\cos\theta')+K_2\cos\frac{\theta'}{2}(\frac{1-3\nu}{1+\nu}+\cos\theta')],\\ \theta_y=&\frac{12(1+\nu)}{Eh^3}\sqrt{\frac{r'}{2}}[K_1\cos\frac{\theta'}{2}(\frac{3-\nu}{1+\nu}-\cos\theta')+K_2\sin\frac{\theta'}{2}(\frac{5+\nu}{1+\nu}+\cos\theta')],\end{aligned} \tag{39}$$

where K_1, K_2, and K_3 denote the moment and shear intensity factors. The origin of the polar coordinate system (r',θ') is placed at the crack tip.

According to the asymptotic displacement field in Eq. (39), the set of CODs $[\Delta\theta_x\ \Delta\theta_y\ \Delta w]^T$ in terms of moment/shear intensity factors between the upper and lower crack surfaces (θ'=180° and θ'=−180°), as illustrated in Fig. 4(a), is given by:

$$\begin{bmatrix}\Delta\theta_x\\ \Delta\theta_y\\ \Delta w\end{bmatrix}=\begin{bmatrix}-\frac{48\sqrt{2r'}}{Eh^3} & 0 & 0\\ 0 & \frac{48\sqrt{2r'}}{Eh^3} & 0\\ 0 & 0 & \frac{24(1+\nu)\sqrt{2r'}}{5Eh}\end{bmatrix}\begin{bmatrix}K_1\\ K_2\\ K_3\end{bmatrix} \tag{40}$$

The set of moment/shear intensity factors $[K_1\ K_2\ K_3]^T$ in terms of CODs can be rewritten as:

$$\begin{bmatrix} K_1 \\ K_2 \\ K_3 \end{bmatrix} = \frac{1}{\sqrt{r'}} \begin{bmatrix} -\frac{Eh^3}{48\sqrt{2}} & 0 & 0 \\ 0 & \frac{Eh^3}{48\sqrt{2}} & 0 \\ 0 & 0 & \frac{5Eh}{24\sqrt{2}(1+\nu)} \end{bmatrix} \begin{bmatrix} \Delta\theta_x \\ \Delta\theta_y \\ \Delta w \end{bmatrix} \tag{41}$$

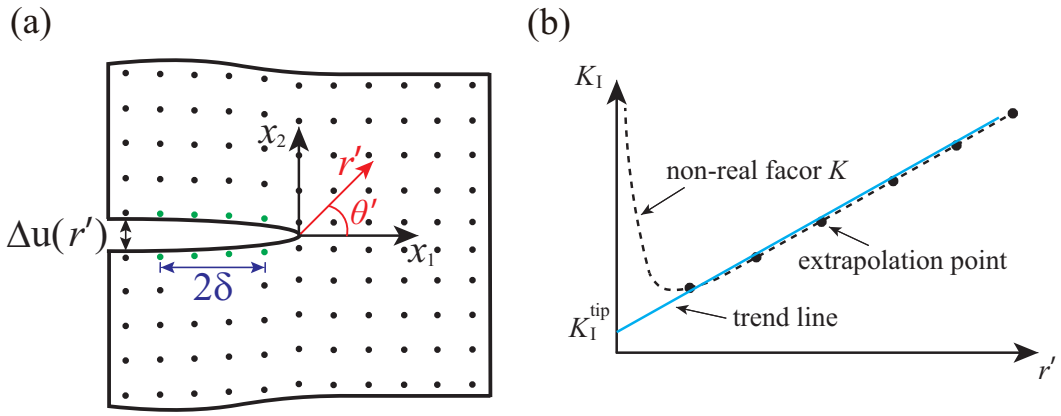

Fig. 4 (a) Schematic illustration of the crack surface displacement extrapolation method, (b) Least-squares approximation for SRIF at the crack tip.

Owing to the singularity of SRIFs in Eq. (41), the extrapolation technique is required to approximate moment/shear intensity factors at the crack tip. Several extrapolation techniques were proposed in the previous studies, including the linear extrapolation [34,38,39], quadratic extrapolation [27], and linear regression [40,41] methods. In the proposed method, the material points within a line segment with distance 2δ along the crack surfaces, as expressed in Fig. 4(a), are selected to be extrapolation points. A linear regression approach, the least-squares method, is applied to evaluate the trend line of SRIF, as illustrated in Fig. 4(b), and then the SRIF value at the crack tip can be obtained.

4 Numerical examples

SIFs and SRIFs are the critical fracture quantities to determine crack extension. The displacement extrapolation method incorporated in the PD Mindlin plate framework is employed to evaluate static and dynamic moment intensity factors. Meanwhile, owing to the influence of the surface effect for the displacement field near crack surfaces, three PD approaches are adopted to examine the effectiveness of the proposed surface effect correction. The standard method without correction, the volume method, and the arbitrary horizon domain method are labeled as Approach 1, Approach 2, and Approach 3, respectively. The volume correction technique [31] is included in all the approaches mentioned above. The horizon size δ is set to $3.015\Delta x$, and the particle spacing of Δx=1/125 m is applied in the following numerical examples with a uniform particle distribution.

The pressure load plays an important role in aerospace and maritime structures. Thus, this study concentrates on the estimation of mode-I moment intensity factors that are the major fracture measures for pressure loads. A commercial FEM software, ABAQUS, is used to compute CODs. Moreover, the reference results of moment intensity factors are determined by substituting CODs obtained from ABAQUS into the displacement extrapolation method [38]. Additionally, the normalized moment intensity factors of F_1=$K_1/M\sqrt{a}$ and F_1=$K_1/p_0(\frac{W}{2})^2\sqrt{a}$ are defined for bending load and pressure load, respectively.

4.1 Square plate with a central crack under static pressure/bending load

A square plate with a central crack under static pressure/bending load is investigated. The length L and width W of the square plate are 2.0 m. Several plate thicknesses of $W/2h$=2, 6, and 10 are considered. Five different crack lengths $2a/W$ are adopted from 0.1 to 0.9 with an equal interval of 0.2. Two loading conditions, including uniform pressure of p_0=1.0 and bending moment of M=1.0, are applied to the square plate with simply supported BCs imposed on the top and bottom edges (see Fig. 5). Young's modulus E and Poisson's ratio ν are set to 1,000 and 0.3, respectively.

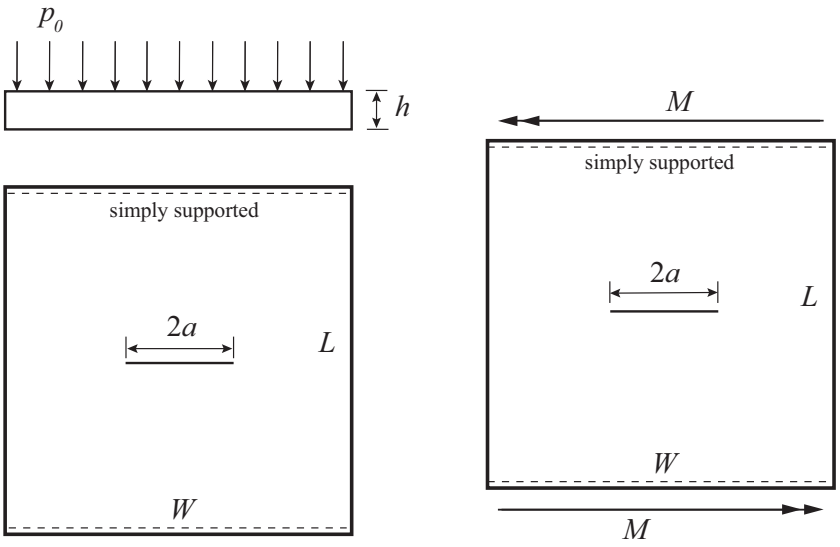

Fig. 5 Square plate with a central crack under static pressure/bending load.

At first, the static fracture behaviors with different configured geometries are investigated to examine the basic performance of the proposed method. The von Mises stress and F_1 results of PD are compared with the FEM and reference [36] solutions, respectively. Those numerical results under pressure load and bending load are expressed in Figs. 6 – 7 and Figs. 8 – 9, respectively. According to the comparisons in Figs. 6 and 8, it confirms that the von Mises stress distributions of $W/2h$=10 and $2a/W$=0.3 match well between PD and FEM. From the comparisons in Figs. 7(a) and 9(a), Approach 3 provides the closest F_1 results of $W/2h$=10 for different crack lengths to the reference solution than Approaches 1 and 2 in both loading conditions. Furthermore, the F_1 results for different plate thicknesses and crack lengths obtained from Approach 3 are in good agreement with those from the reference solution in both loading conditions (see Figs. 7(b) and 9(b)).

4.2 Square plate with a central crack under dynamic pressure load

A square plate with a central crack under dynamic pressure load is analyzed. The length L, width W, and thickness h of the square plate are 2.0, 2.0, and 0.1 m, respectively. The half crack length a is set to 0.1 m. The square plate is subjected to a uniform pressure of $p_0H(t)$=1.0 MPa; here, $H(t)$ denotes the Heaviside step function. Meanwhile, two different displacement BCs are imposed on all the edges, including clamped BCs and simply supported BCs (see Fig. 10). Young's modulus E, Poisson's ratio ν, and density ρ are set to 200 GPa, 0.3, and 7,850 kg/m^3, respectively.

The displacement and dynamic F_1 results for two different displacement BCs are compared between the PD and FEM solutions. Those numerical results under clamped BCs and simply supported BCs are presented in Figs. 11 and 12, respectively. From the comparisons in Figs. 11(a) and 12(a), the displacement results nearby the crack tip agree well between Approach 3 and FEM in both displacement

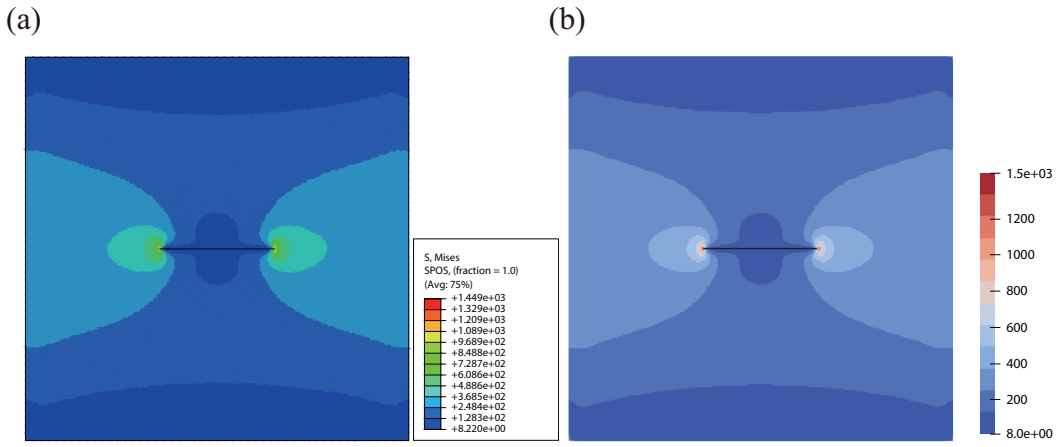

Fig. 6 von Mises stress distribution (Pa) of $W/2h$=10 and $2a/W$=0.3 under static pressure load, (a) FEM, (b) PD.

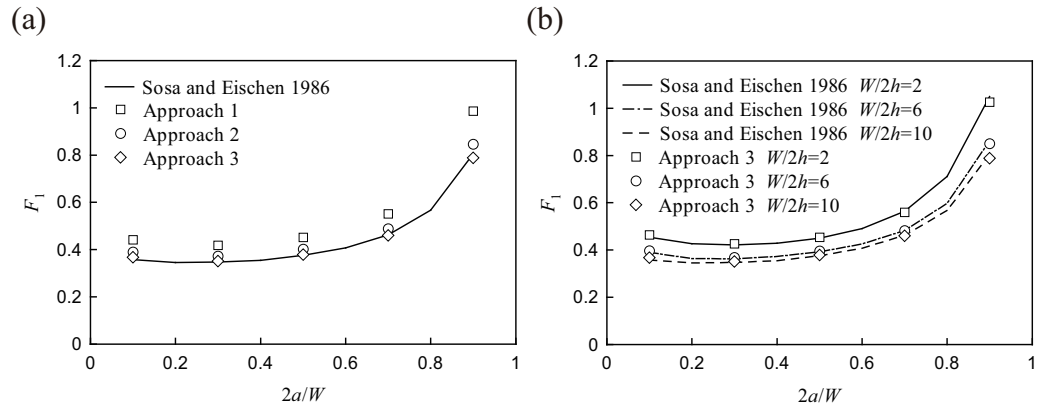

Fig. 7 SRIF evaluation under static pressure load, (a) Normalized moment intensity factor of $W/2h$=10 for different PD approaches, (b) Normalized moment intensity factor for different plate thicknesses.

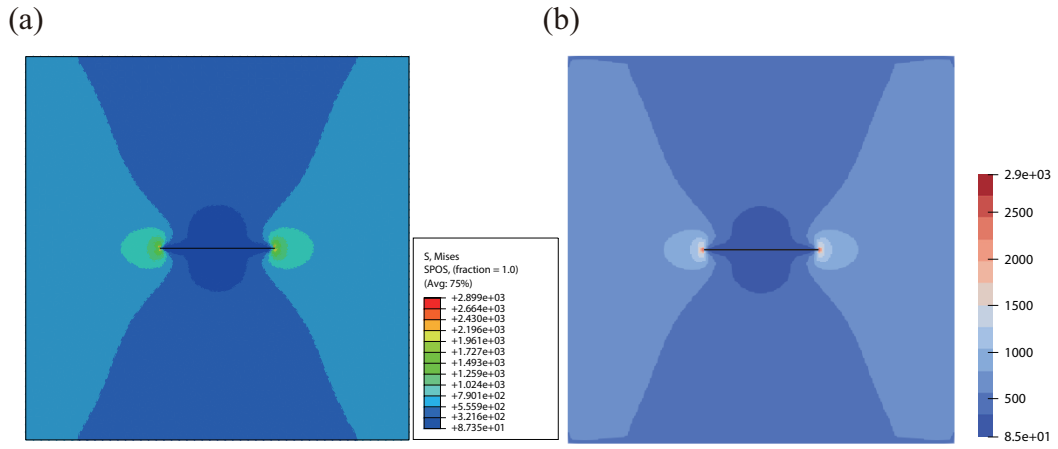

Fig. 8 von Mises stress distribution (Pa) of $W/2h$=10 and $2a/W$=0.3 under static bending load, (a) FEM, (b) PD.

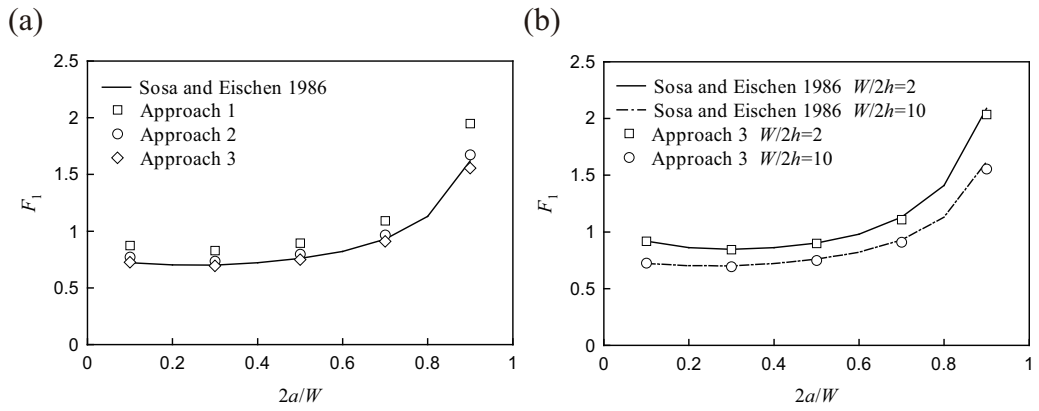

Fig. 9 SRIF evaluation under static bending load, (a) Normalized moment intensity factor of $W/2h$=10 for different PD approaches, (b) Normalized moment intensity factor for different plate thicknesses.

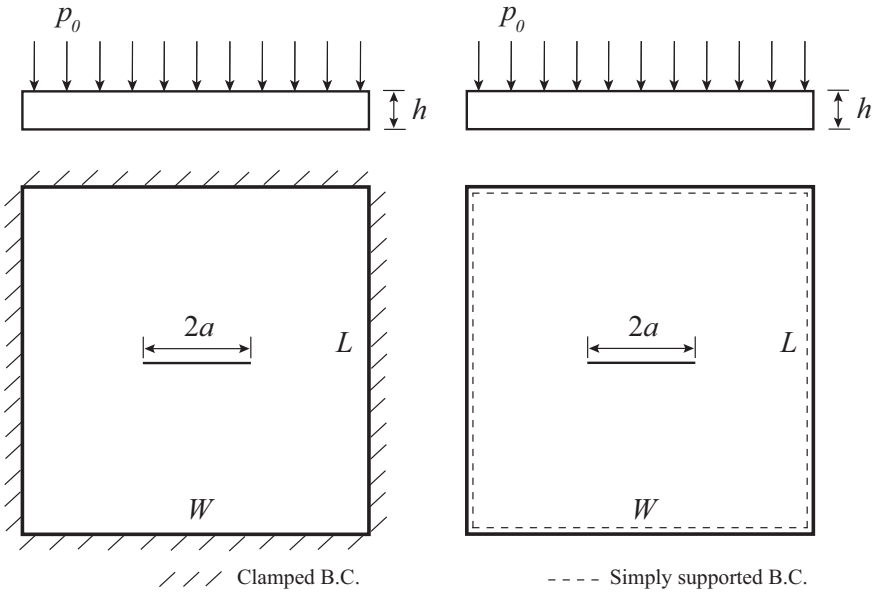

Fig. 10 Square plate with a central crack under dynamic pressure load with clamped/simply supported BCs.

BC conditions. Moreover, the dynamic F_1 results of Approach 3 are closest to those of FEM than Approaches 1 and 2 in both displacement BC conditions (see Figs. 11(b) and 12(b)).

4.3 Rectangular plate with an edge crack under dynamic pressure load

A rectangular plate with an edge crack under dynamic pressure load is conducted. The length L, width W, and thickness h of the rectangular plate are 1.0, 2.0, and 0.1 m, respectively. The crack length a is set to 0.5 m. The rectangular plate is subjected to a uniform pressure of $p_0H(t)$=1.0 MPa with clamped BCs imposed on the right and left edges (see Fig. 13). Young's modulus E, Poisson's ratio ν, and density ρ are set to 200 GPa, 0.3, and 7,850 kg/m^3, respectively.

Similarly, the displacement and dynamic F_1 results are compared between the PD and FEM solutions. The displacement results nearby the crack tip illustrated in Fig. 14(a) match well between Approach 3 and FEM. In addition, from the comparison between three PD approaches and FEM, the dynamic F_1 results of Approach 3 are most similar to those of FEM (see Figs. 14(b)).

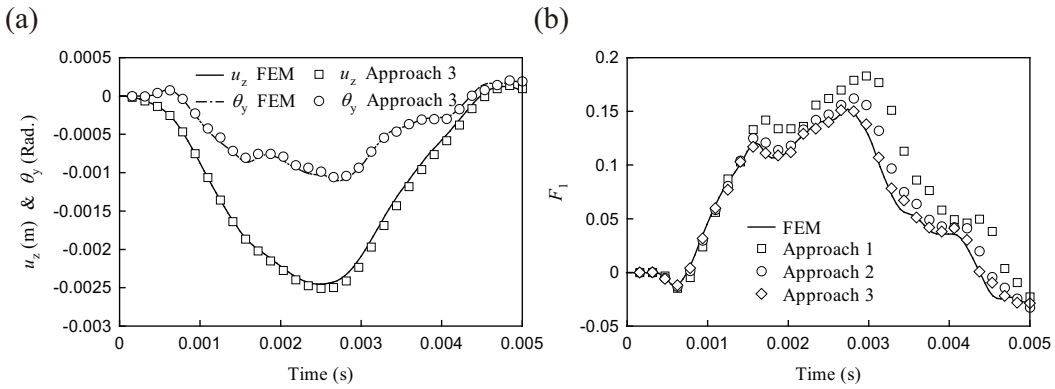

Fig. 11 Fracture behaviors of the square plate with clamped BCs, (a) Displacement u_z and rotation θ_y nearby the crack tip, (b) Normalized moment intensity factor for different PD approaches.

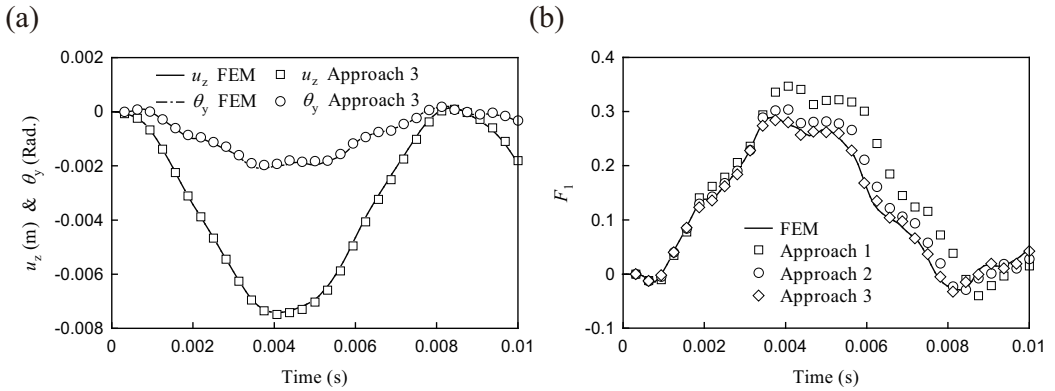

Fig. 12 Fracture behaviors of the square plate with simply supported BCs, (a) Displacement u_z and rotation θ_y nearby the crack tip, (b) Normalized moment intensity factor for different PD approaches.

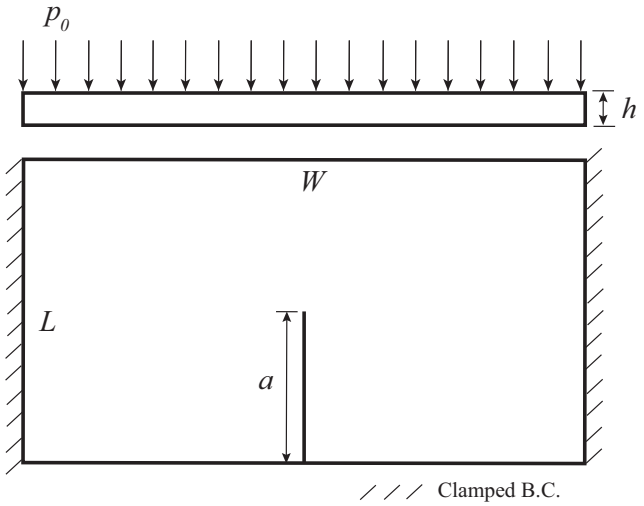

Fig. 13 Rectangular plate with an edge crack under dynamic pressure load.

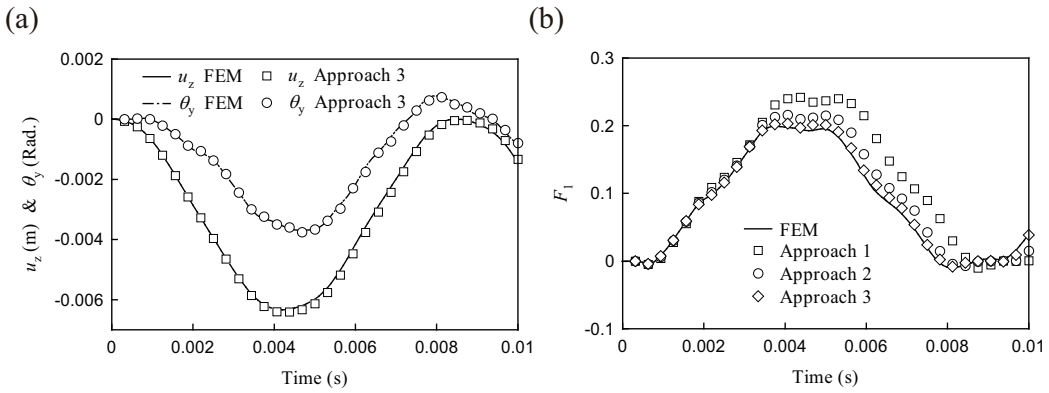

Fig. 14 Fracture behaviors of the rectangular plate, (a) Displacement u_z and rotation θ_y nearby the crack tip, (b) Normalized moment intensity factor for different PD approaches.

4.4 Square plate with a side crack/two symmetric cracks emanating from a central hole under dynamic pressure load

A square plate with a side crack/two symmetric cracks emanating from a central hole under dynamic pressure load is performed. The length L, width W, and thickness h of the square plate are 2.0, 2.0, and 0.1 m, respectively. The circle hole is located at the center of the square plate, and its radius is set to 0.15 m. The crack length a emanating from the central hole is set to 0.15 m. The square plate is subjected to a uniform pressure of $p_0H(t)$=1.0 MPa with clamped BCs imposed on the top and bottom edges (see Fig. 15). Young's modulus E, Poisson's ratio ν, and density ρ are set to 200 GPa, 0.3, and 7,850 kg/m^3, respectively.

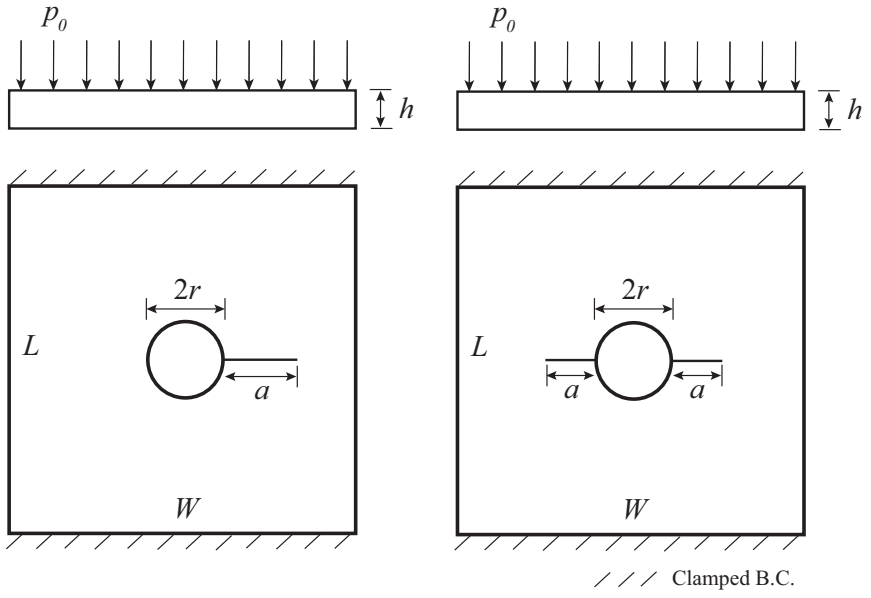

Fig. 15 Square plate with a side crack/two symmetric cracks emanating from a central hole under dynamic pressure load.

Here, the displacement and dynamic F_1 results for two different crack configurations are compared between the PD and FEM solutions. Those numerical results with a side crack and two symmetric

cracks are plotted in Figs. 16 and 17, respectively. According to the comparisons in Figs. 16(a) and 17(a), the displacement results nearby the crack tip between Approach 3 and FEM have a good agreement in both crack configurations. Additionally, the comparisons of dynamic F_1 results indicate that the results of Approach 3 are most analogous to those of FEM rather than Approaches 1 and 2 in both crack configurations (see Figs. 16(b) and 17(b)).

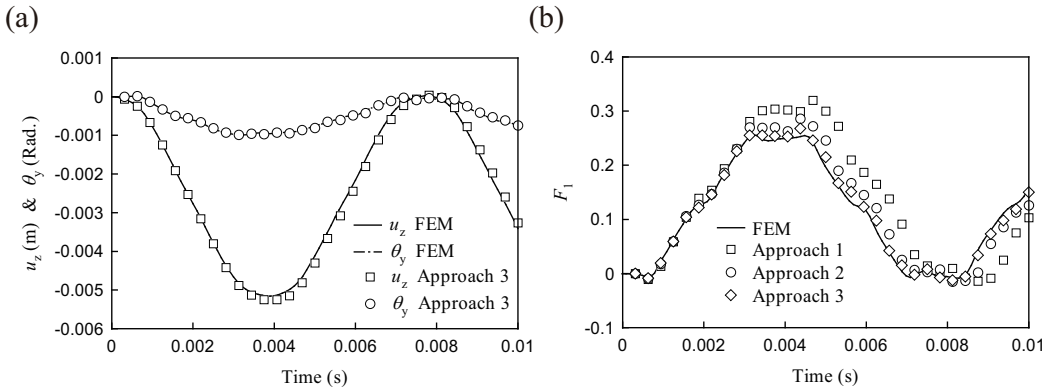

Fig. 16 Fracture behaviors of the square plate with a side crack, (a) Displacement u_z and rotation θ_y nearby the crack tip, (b) Normalized moment intensity factor for different PD approaches.

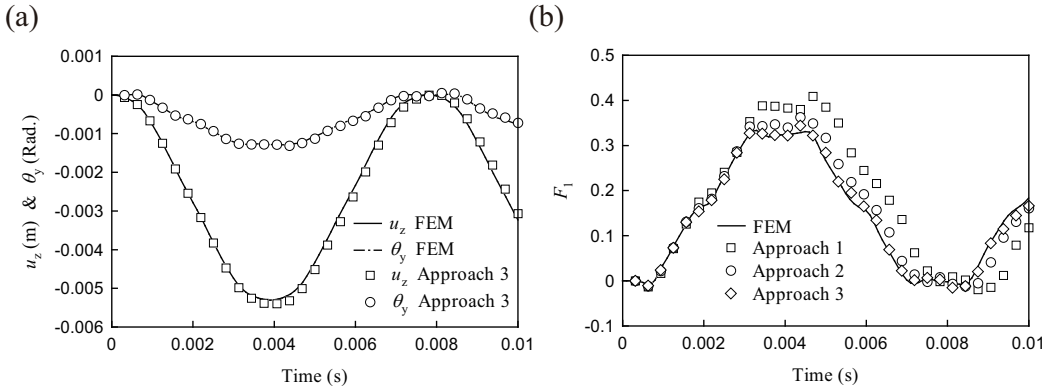

Fig. 17 Fracture behaviors of the square plate with two symmetric cracks, (a) Displacement u_z and rotation θ_y nearby the crack tip, (b) Normalized moment intensity factor for different PD approaches.

5 Conclusion

SIFs and SRIFs are regarded as the major fracture parameters to determine crack extension. However, few SRIF studies for plate bending problems, especially dynamic analysis, have been carried out in the PD literature. Therefore, the Mindlin plate model in the OSPD framework is presented to treat fracture mechanics problems for plate structures. The displacement extrapolation method is adopted to compute static and dynamic moment intensity factors. Owing to the PD surface effect, the accuracy of the displacement field near crack surfaces is significantly affected. To minimize the influence from the surface effect, the arbitrary horizon domain method is employed. The proposed surface effect correction derives the variable PD parameters to properly reproduce mechanical behaviors for each material point.

Several numerical examples are considered to assess fracture behaviors near the crack tip. At first, the static estimations of moment intensity factors under two different loading conditions are investigated to confirm the basic performance of the proposed method. Since the pressure load is the major loading mode for aerospace and maritime structures, hereafter, the dynamic estimations of displacements and moment intensity factors subjected to a uniform pressure load are analyzed. Those numerical results are compared between PD and FEM. Although the stress singularity arises near the crack tip in FEM, it can provide accurate results in the displacement field. Thus, FEM is chosen to compute the reference results in the present study. From the comparisons mentioned in Section 4, it indicates that the displacement extrapolation method incorporated with the arbitrary horizon domain method can successfully minimize the PD surface effect and properly assess fracture behaviors for plate bending problems in the PD Mindlin plate framework. It is believed that the accurate fracture behaviors near the crack tip assessed by the proposed method can improve the capability of the OSPD theory to simulate crack propagation.

A Examination of boundary conditions in the nonlocal theory

The peridynamic method regarded as a nonlocal continuum theory requires some special treatments to impose boundary conditions, such as the weak form of peridynamics [42], the modified fictitious node method [43], and the variable horizon method [44]. In the present paper, volumetric regions (nonlocal boundary) are employed to implement external load and constraint boundary conditions (see Chap. 2 in Ref. [31]). For external load boundary conditions, the external load computed as body force density is applied on a real material layer along the boundary possessing nonzero volume. For constraint boundary conditions, the prescribed constraint is adopted on a fictitious layer with the particular length scale, δ, outside the physical boundary. Several numerical examples with constraint boundary conditions are successfully examined in Section 4. In Appendix A, a numerical example with external load and constraint boundary conditions is investigated.

A cantilever square plate with a central crack under dynamic transverse shear load is carried out. The length L, width W, and thickness h of the square plate are 2.0, 2.0, and 0.1 m, respectively. The half crack length a is set to 0.1 m. The square plate is subjected to a transverse shear force of $QH(t)$=1.0 MPa on the right edge with clamped BCs imposed on the left edge (see Fig. 1). Young's modulus E, Poisson's ratio ν, and density ρ are set to 200 GPa, 0.3, and 7,850 kg/m^3, respectively.

As illustrated in Fig. 2(a) and (b), the displacement nearby the crack tip and dynamic F_1 results are in good agreement between the PD and FEM solutions. It demonstrates that the proposed nonlocal method can well simulate fracture behaviors under different types of boundary conditions.

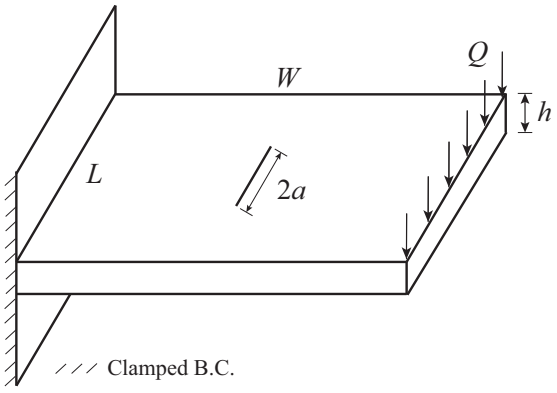

Fig. 1 Cantilever square plate with a central crack under dynamic transverse shear load.

Acknowledgements

The first author gratefully acknowledges financial support from Japan–Taiwan Exchange Association.

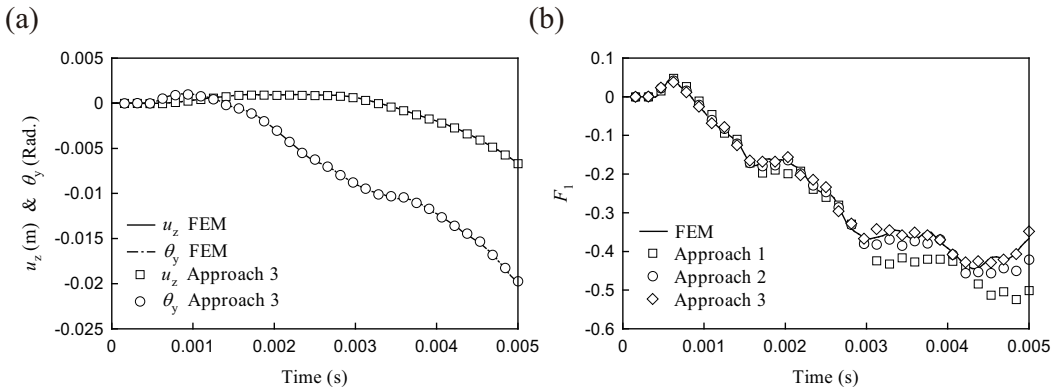

Fig. 2 Fracture behaviors of the cantilever square plate, (a) Displacement u_z and rotation θ_y nearby the crack tip, (b) Normalized moment intensity factor for different PD approaches.

References

1. Silling, S.A.: Reformulation of elasticity theory for discontinuities and long-range forces. J. Mech. Phys. Solids **48**, 175-209 (2000)
2. Silling, S.A., Epton, M., Weckner, O., Xu, J., Askari, E.: Peridynamic states and constitutive modeling. J. Elast. **88**, 151-184 (2007)
3. O'Grady, J., Foster, J.: Peridynamic plates and flat shells: A non-ordinary, state-based model. Int. J. Solids Struct. **51**, 4572-4579 (2014)
4. O'Grady, J., Foster, J.: A meshfree method for bending and failure in non-ordinary peridynamic shells. Comput. Mech. **57**, 921-929 (2016)
5. Diyaroglu, C., Oterkus, E., Oterkus, S., Madenci, E.: Peridynamics for bending of beams and plates with transverse shear deformation. Int. J. Solids Struct. **69 — 70**, 152-168 (2015)
6. Chowdhury, S.R., Roy, P., Roy, D., Reddy, J.N.: A peridynamic theory for linear elastic shells. Int. J. Solids Struct. **84**, 110-132 (2016)
7. Nguyen, C.T., Oterkus, S.: Peridynamics for the thermomechanical behavior of shell structures. Eng. Fract. Mech. **219**, 106623 (2019)
8. Yang, Z., Vazic, B., Diyaroglu, C., Oterkus, E., Oterkus, S.: A Kirchhoff plate formulation in a state-based peridynamic framework. Math. Mech. Solids **25**, 727-738 (2020)
9. Yang, Z., Oterkus, E., Oterkus, S.: Peridynamic formulation for higher-order plate theory. J. Peridyn. Nonlocal Model. 1-26 (2020)
10. Zhang, Q., Li, S., Zhang, A., Peng, Y., Yan, J.: A peridynamic Reissner-Mindlin shell theory. Int. J. Numer. Methods Eng. **122**, 122-147 (2021)
11. Nguyen, C.T., Oterkus, S.: Ordinary state-based peridynamics for geometrically nonlinear analysis of plates. Theor. Appl. Fract. Mech. **112**, 102877 (2021)
12. Shen, G., Xia, Y., Hu, P., Zheng, G.: Construction of peridynamic beam and shell models on the basis of the micro-beam bond obtained via interpolation method. Eur. J. Mech. A Solids **86**, 104174 (2021)
13. Shen, G., Xia, Y., Li, W., Zheng, G., Hu, P.: Modeling of peridynamic beams and shells with transverse shear effect via interpolation method. Comput. Methods Appl. Mech. Eng. **378**, 113716 (2021)
14. Zhang, Q., Li, S., Zhang, A., Peng, Y.: On nonlocal geometrically exact shell theory and modeling fracture in shell structures. Comput. Methods Appl. Mech. Eng. **386**, 114074 (2021)
15. Le, Q.V., Bobaru, F.: Surface corrections for peridynamic models in elasticity and fracture. Comput. Mech. **61**, 499-518 (2018)
16. Queiruga, A.F., Moridis, G.: Numerical experiments on the convergence properties of state-based peridynamic laws and influence functions in two-dimensional problems, Comput. Methods Appl. Mech. Eng. **322**, 97-122 (2017)
17. Chen, K.C.: The development of coupled peridynamics and iso-geometric analysis method for modeling of crack propagation on ship-hull panels. Master Thesis, National Taiwan Ocean University (2020) (in Chinese)
18. Dai, M.J., Tanaka, S., Guan, P.C., Oterkus, S., Oterkus, E.: Ordinary state-based peridynamic shell model with arbitrary horizon domains for surface effect correction. Theor. Appl. Fract. Mech. **115**, 103068 (2021)
19. Silling, S.A., Lehoucq, R.B.: Peridynamic theory of solid mechanics. Adv. Appl. Mech. **44**, 73-168 (2010)
20. Hu, W., Ha, Y.D., Bobaru, F., Silling, S.A.: The formulation and computation of the nonlocal J-integral in bond-based peridynamics. Int. J. Fract. **176**, 195-206 (2012)
21. Stenström, C., Eriksson, K.: The J-contour integral in peridynamics via displacements. Int. J. Fract. **216**, 173-183 (2019)
22. Stenström, C., Eriksson, K.: The J-area integral applied in peridynamics. Int. J. Fract. **228**, 127-142 (2021)
23. Imachi, M., Tanaka, S., Bui, T.Q.: Mixed-mode dynamic stress intensity factors evaluation using ordinary state-based peridynamics. Theor. Appl. Fract. Mech. **93**, 97-104 (2018)

24. Imachi, M., Takei, T., Ozdemir, M., Tanaka, S., Oterkus, S., Oterkus, E.: A smoothed variable horizon peridynamics and its application to the fracture parameters evaluation. Acta Mech. **232**, 533-553 (2021)
25. Dai, M.J., Tanaka, S., Oterkus, S., Oterkus, E.: Mixed-mode stress intensity factors evaluation of flat shells under in-plane loading employing ordinary state-based peridynamics. Theor. Appl. Fract. Mech. **112**, 102841 (2021)
26. Dai, M.J., Tanaka, S., Bui, T.Q., Oterkus, S., Oterkus, E.: Fracture parameter analysis of flat shells under out-of-plane loading using ordinary state-based peridynamics. Eng. Fract. Mech. **244**, 107560 (2021)
27. Areias, P.M.A., Belytschko, T.: Non-linear analysis of shells with arbitrary evolving cracks using XFEM. Int. J. Numer. Methods Eng. **62**, 384-415 (2005)
28. Li, J., Khodaei, Z.S., Aliabadi, M.H.: Dynamic dual boundary element analyses for cracked Mindlin plates. Int. J. Solids Struct. **152 – 153**, 248-260 (2018)
29. Bobaru, F., Foster, J.T., Geubelle, P.H., Silling, S.A.: Handbook of peridynamic modeling. CRC Press Taylor & Francis Group, Boca Raton (2016)
30. Kilic, B., Madenci, E.: An adaptive dynamic relaxation method for quasi-static simulations using the peridynamic theory. Theor. Appl. Fract. Mech. **53**, 194-204 (2010)
31. Madenci, E., Oterkus, E.: Peridynamic theory and its applications. Springer, New York (2014)
32. Underwood, P.: Dynamic relaxation. Comput. Meth. Trans. Anal. **1**, 245-265 (1983)
33. Liu, Z., Ye, H., Qian, D., Zhang, H., Zheng, Y.: A time-discontinuous peridynamic method for transient problems involving crack propagation. Int. J. Numer. Methods Eng. **122**, 1824-1845 (2020)
34. Dirgantara, T., Aliabadi, M.H.: Dual boundary element formulation for fracture mechanics analysis of shear deformable shells. Int. J. Solids Struct. **38**, 7769-7800 (2001)
35. Belytschko, T., Lu, Y.Y., Gu, L.: Element-free Galerkin methods. Int. J. Numer. Methods Eng. **37**, 229-256 (1994)
36. Sosa, H.A., Eischen, J.: Computation of stress intensity factors for plate bending via a path-independent integral. Eng. Fract. Mech. **25**, 451-462 (1986)
37. Dolbow, J., Moës, N., Belytschko, T.: Modeling fracture in Mindlin-Reissner plates with the extended finite element method. Int. J. Solids Struct. **37**, 7161-7183 (2000)
38. Guinea, G.V., Planas, J., Elices, M.: K_{I} evaluation by the displacement extrapolation technique. Eng. Fract. Mech. **66**, 243-255 (2000)
39. Zhu, N., Oterkus, E.: Calculation of stress intensity factor using displacement extrapolation method in peridynamic framework. J. Mech. **36**, 235-243 (2020)
40. Han, Q., Wang, Y., Yin, Y., Wang, D.: Determination of stress intensity factor for mode I fatigue crack based on finite element analysis. Eng. Fract. Mech. **138**, 118-126 (2015)
41. Qian, G., González-Albuixech, V.F., Niffenegger, M., Giner, E.: Comparison of K_{I} calculation methods. Eng. Fract. Mech. **156**, 52-67 (2016)
42. Madenci, E., Dorduncu, M., Barut, A., Phan, N.: Weak form of peridynamics for nonlocal essential and natural boundary conditions. Comput. Methods Appl. Mech. Eng. **337**, 598-631 (2018)
43. Scabbia, F., Zaccariotto, M., Galvanetto, U.: A novel and effective way to impose boundary conditions and to mitigate the surface effect in state-based Peridynamics. Int. J. Numer. Methods Eng. **122**, 5773-5811 (2021)
44. Prudhomme, S., Diehl, P.: On the treatment of boundary conditions for bond-based peridynamic models. Comput. Methods Appl. Mech. Eng. **372**, 113391 (2020)